Title

Dynamics of resonant low-energy electron attachment to ethanol-producing hydroxide anions

Journal

Physical Review A, 108(5)

ISSN

2469-9926

Authors

Chakraborty, Dipayan

Slaughter, Daniel S

Ptasinska, Sylwia

Publication Date

2023-11-01

DOI

10.1103/physreva.108.052806

Dynamics of resonant low energy electron attachment to ethanol producing hydroxide anions.

Dipayan Chakraborty[a,*], Daniel S. Slaughter[b], and Sylwia Ptasinska[a,c]
[a] *Radiation Laboratory, University of Notre Dame, Notre Dame, Indiana 46556, United States,*
[b] *Lawrence Berkeley National Laboratory, Chemical Sciences, Berkeley, California 94720, United States, and*
[c] *Department of Physics & Astronomy, University of Notre Dame, Notre Dame, IN 46556, USA**
(Dated: November 14, 2023)

Dynamics of dissociative electron attachment to ethanol is experimentally investigated at the Feshbach resonance formed with incident electron energies near 9.5 eV. Highly differential laboratory-frame momentum distributions of OH^- fragments are measured, for a series of energies spanning the resonance width, using the velocity map imaging (VMI) technique. The OH^- kinetic energy distribution indicates that the C-O breaking dissociation process could either be a three-body dissociation or a two-body dissociation with significant rovibrational excited fragments. The small but significant anisotropy in the OH^- angular distribution provides signatures of the molecular symmetry of the associated resonant state under the axial recoil approximation, which assumes the dissociation is much faster than any rotation of the dissociation axis. Within these assumptions, the 9.5 eV Feshbach resonance can be assigned to the electronic transition from the $(10a^{'})$ orbital with its ground state C_s symmetry to the empty $(4a^{''})$ level, involving the simultaneous electron attachment. This dynamics could be a model for C-O dissociation in larger alcohols and ethers.

PACS numbers: 34.80.Gs, 34.80.Ht

I. INTRODUCTION

Dissociative electron attachment (DEA) is one of a few important fundamental processes that allow low-energy electrons to initiate the fragmentation of molecules into reactive anions and radicals [1–4]. In DEA, a transient negative ion (TNI) resonance is formed by electron attachment, and the TNI may dissociate if the resonance exists for sufficient time before autodetachment occurs [5]. Feshbach resonances [6] are electronic states of TNIs that cannot autoionize by an electronic transition involving a single electron. These core-excited TNI resonances are established to play an important role in DEA [7–9], but they present significant challenges, even to highly sophisticated theoretical methods, due to the demands of an accurate description of electronic correlation to determine the potential energy and energy width of the resonance. Experimental measurements of the resonance energy, DEA ion yield, fragment kinetic energy, and/or angular distributions have proven to provide valuable information on Feshbach resonances.

Feshbach resonances are common in alcohols and have been reported for a broad range of energies as low as a few eV below the ionization potential. Several theoretical and experimental studies have been conducted over the years to understand the dynamics of Feshbach resonances involved in the electron attachment to methanol, the simplest alcohol [10, 11]. Curtis and Walker [10] compared the DEA ion yields of methanol with the corresponding parent Rydberg states in both VUV (vacuum ultraviolet) photoabsorption spectra and near-threshold electron energy-loss spectra. They found that the 6.5 and 8 eV Feshbach resonances in methanol are due to the transition of an electron from either of the two ground-state highest-lying occupied orbitals, $(7a^{'})^2$ or $(2a^{''})^2$ to the $3s$ Rydberg orbital, which is also occupied by the attached electron. They also established that the 6.5 and 8 eV resonances have $^2A^{''}$ and $^2A^{'}$ symmetry, respectively. Later, adopting anion fragment momentum imaging, Slaughter *et al.* [11] confirmed the $^2A^{''}$ symmetry of the 6.5 eV Feshbach resonance.

Similarly, low-energy electron resonances at 9.5 eV leading to OH^- release from ethanol is categorized as a Feshbach resonance since it is near and below the ionization energy (IE) of ethanol, 10.64 eV [12]. Several experimental attempts have been made over the years to determine the dynamics involved in the ethanol molecule's Feshbach resonances, but no conclusive evidence has been documented to date. By studying the D^- ion yield from deuterated ethanol and H-loss channel, Ibănescu *et al.* [13, 14] suggested that the Feshbach resonance near 6.35 eV is due to a hole in the n_O lone pair orbital, and the 7.85 eV is due to a hole in the $\bar{n}_O$ lone pair orbital. Further, the broad 9.15 eV Feshbach resonance was attributed to the promotion of a bound electron from various C-H and C-C σ orbitals. Ibănescu *et al.* [15] also compared the DEA spectra with the vibrational excitation (VE) spectrum of the C-H and O-H stretching modes, as the VE cross-section is generally enhanced by resonances, particularly by shape resonances and vibrational Feshbach resonances. In the absence of clear correlations between the VE spectrum and the DEA resonances, the authors concluded that the 6.35, 7.85, and 9.15 eV resonances are core-excited Feshbach resonances. Moreover, Orzol *et al.* [16] performed a combined gas-phase and condensed-phase DEA studies, in which the

* dchakra2@nd.edu

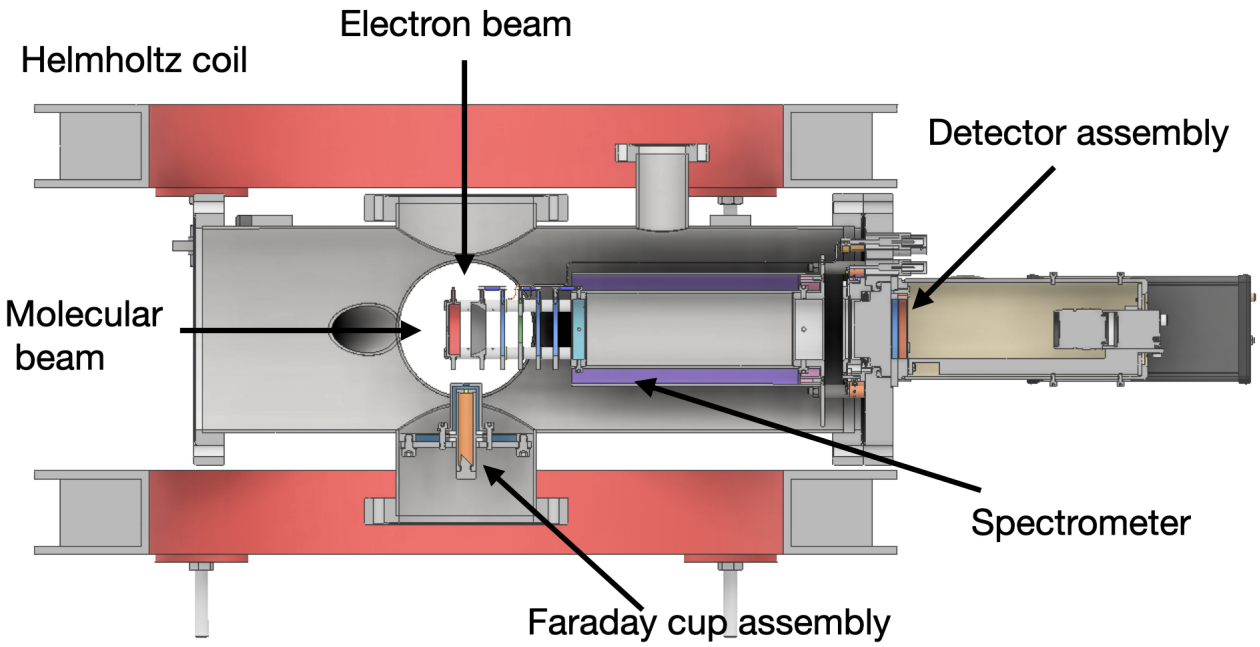

FIG. 1. Schematic view of the experimental set-up, which consists of the vacuum chamber, spectrometer, Faraday cup assembly, detector assembly, and Helmholtz coils. The electron gun is attached to the top flange, and the needle that produces the effusive molecular beam is attached to the flange on the left as indicated by the direction of a molecular beam.

different fragmentation channels and their corresponding ion-yield curves were reported. Later, using the R-matrix calculations, Fujimoto *et al.* [17] predicted the presence of broad shape resonances near the 7.5 and 8 eV regions with the $^2A''$ and $^2A'$ symmetries, respectively. However, their model was not able to provide the data on the Feshbach resonances at energies near the electronic excitation thresholds, which are dominant in the DEA channel observed in the 9.5 eV region. Later, Wang *et al.* [18] investigated DEA to ethanol using a velocity map imaging (VMI) spectrometer. Their combined theoretical and experimental investigations indicate that initially, a Feshbach resonance is formed by vertical electron attachment, then it couples with a σ^* shape resonance which is responsible for H loss from the TNI. However, the mechanism for the C-OH dissociation channel is still unknown. In particular, while there is some evidence [13] that more than one resonance contributes to DEA around 9.5 eV, limited information can be extracted from measurements of energy-dependent fragment yields alone. Therefore, we expect energy and angle-differential fragment imaging of OH^- to offer further insight into the nature of the resonance(s).

In this framework, the present study focuses on understanding the electronic transition involved in the 9.5 eV Feshbach resonance along with the associated dissociation dynamics of the TNI electronic state leading to the production of hydroxide, OH^-. The VMI images of the OH^- ions were recorded to obtain both the kinetic energy and angular distributions for a series of electron energies at and near the resonance peak. Anion fragment angular distributions are understood to contain information on the electron attachment dynamics and/or on the dissociation dynamics. Using the axial recoil approximation, we assume the dissociation axis does not rotate significantly during the dissociation process, which allows us to determine the symmetry of the TNI. Furthermore, we consider the possible failure of the axial recoil approximation by rotation of the C-O bond to discuss the possible dissociation dynamics revealed in the VMI images.

We applied the time-sliced VMI technique using an apparatus that was recently designed and constructed in the Notre Dame Radiation Laboratory. The cross-sectional view of the custom-designed experimental setup is shown in Fig. 1. It consists of an electron gun, a Faraday cup to measure the electron beam current, an effusive molecular beam, a time of flight (TOF)-based VMI spectrometer, and a microchannel plate (MCP)-based detector assembly with a position-sensitive phosphor anode. The electron gun is purchased from Kimball Physics (Model No: ELG-2/EGPS-1022), and the detector assembly is purchased from Photek USA. The electron gun consists of a resistively heated tantalum filament that produces an electron beam with a typical resolution of 0.6 eV, defined as the full width at half maximum (FWHM) of the electron energy distribution. A pair of Helmholtz coils with a diameter of 556 mm is placed outside the vacuum chamber to

produce a uniform magnetic field to collimate and guide the low-energy electron beam. The spectrometer consists of repeller and extractor plate electrodes, a lens assembly, and a drift tube. The repeller and extractor plates, each with 60 mm outer diameter, are separated by 20 mm. A stainless-steel capillary, 550 μm inner diameter, is used to produce the effusive molecular beam, and the typical distance between the exit of the capillary and the electron beam is around 3 mm. Electron-molecule interaction occurs between the repeller and extractor plates. On the repeller plate, a negative pulse is applied to push the negative ions. The extractor plate is typically grounded. At about 13 mm from the extractor plate, four lens electrodes (60 mm in diameter, each) are placed. The separation between each pair of lens electrodes is 10 mm. These lens electrodes are mainly used to focus the negative ions. After the lens electrodes, a 185 mm long field-free drift tube is placed. At the end of the drift tube, two MCP plates in chevron configurations are placed. The effective diameter of the MCP plates is 40 mm. The drift tube and the front MCP plate are at the same potential. At the end of the MCP plates, one phosphor screen is placed. Behind the phosphor screen, a charge-coupled device (CCD) camera is placed to capture the image.

The basic procedure in the experiment entailed applying a pulsed electron beam for 200 ns with a 5 kHz repetition rate. The electron beam passed through the interaction region, where it collided with the molecular beam to produce DEA fragments. After the electron-beam pulse, a negative 150 V amplitude pulse with a 150 ns delay is applied to the repeller plate to push the negative ions from the interaction region into the VMI spectrometer. The delayed extraction results in a better kinetically resolved time-sliced image and also prevents the electrons from reaching the detector. The spectrometer is designed to maintain the VMI condition, i.e., all the ions with a given velocity vector are mapped onto a single point on the detector regardless of their origin. The experiments were performed under ultra-high vacuum conditions with a base pressure as low as 10^{-9} mbar (working pressure $\sim 5 \times 10^{-7}$mbar) and using 99.5% pure ethanol purchased from Sigma Aldrich, USA.

A molecule in the molecular beam can be oriented in any arbitrary direction in free space. Negative ions produced by DEA are contained within an expanding sphere, referred to as a Newton sphere. The kinetic energy distribution (KED) and angular distribution of the negative ions can be obtained from the projection of the Newton sphere onto the detector. Ions with higher kinetic energy fall onto the detector, forming an image with a larger diameter. The obtained central slice of the Newton sphere contains the initial kinetic energy and angular distribution information of the detected ions. A 50 ns time-sliced image was recorded from the central area of the entire Newton sphere. To obtain the central slice, a gate module to pulse the rear MCP plate was used. A transistor-transistor logic pulse generator with an appropriate delay is used to trigger the gate module. These sliced images represent distributions of ions that have the initial momentum in the plane parallel to the detector. The electron energy calibration was performed using the resonant peaks of O^- ion yields from DEA to carbon dioxide at 4 eV, and oxygen at 6.5 eV [19]. The kinetic energy distribution measurements were calibrated using the kinetic energy released by the O^- ions from O_2 around the same energy [20] as shown in Fig. 2d. Further, this energy calibration was confirmed by measuring the kinetic energy of the O^- ion produced by dissociative electron attachment to CO_2 at 8.2 eV [21], as shown in Fig. 2b. The information on the electron beam axis was also obtained from the momentum image from DEA to CO_2 molecule at 8.2 eV [21] as shown in Fig. 2a.

The signal detected on the screen is also used for the measurement of ion yield curves of the negative ions. First, the AC-coupled screen signal is amplified by a fast amplifier and then fed to a constant fraction discriminator (CFD). The CFD output is connected to the STOP of a nuclear instrumentation module standard time to amplitude converter (TAC), and the START pulse is generated by a master pulse generator that is synchronized with the electron gun pulse. The time difference between this START and STOP is the TOF of the negative ions. The output of the TAC is connected to a multichannel analyzer. Finally, it is communicated to a computer via a USB 2.0 interface for data acquisition. A custom-built LabVIEW-based data acquisition system was used to obtain the mass spectra and ion yield curves.

II. ANGULAR DISTRIBUTION OF OH^-

The OH^- angular distribution is measured in the laboratory frame of reference, which is defined by the electron beam direction. The molecular frame is not directly accessible in the present experiments because the target molecules have random orientations in the molecular beam. In smaller molecules, *ab initio* electron scattering calculations have been performed to accurately predict the electron attachment cross-section in the molecular frame [7]. However, for more complex molecules, analysis of the dynamics of DEA typically demands accurate electron attachment theoretical calculations, or some prior knowledge or assumptions about the resonant states, or the dissociation dynamics. Such a computationally expensive approach is beyond the scope of the present experimental study. Therefore, we assume the axial recoil approximation to discuss the possible resonance symmetries. Then we will consider the breakdown of the axial recoil approximation.

Azria *et al.* [22] extended the electron attachment theory of O'Malley and Taylor [23], and Dunn [24] to polyatomic molecules, in which the general form of the transition am-

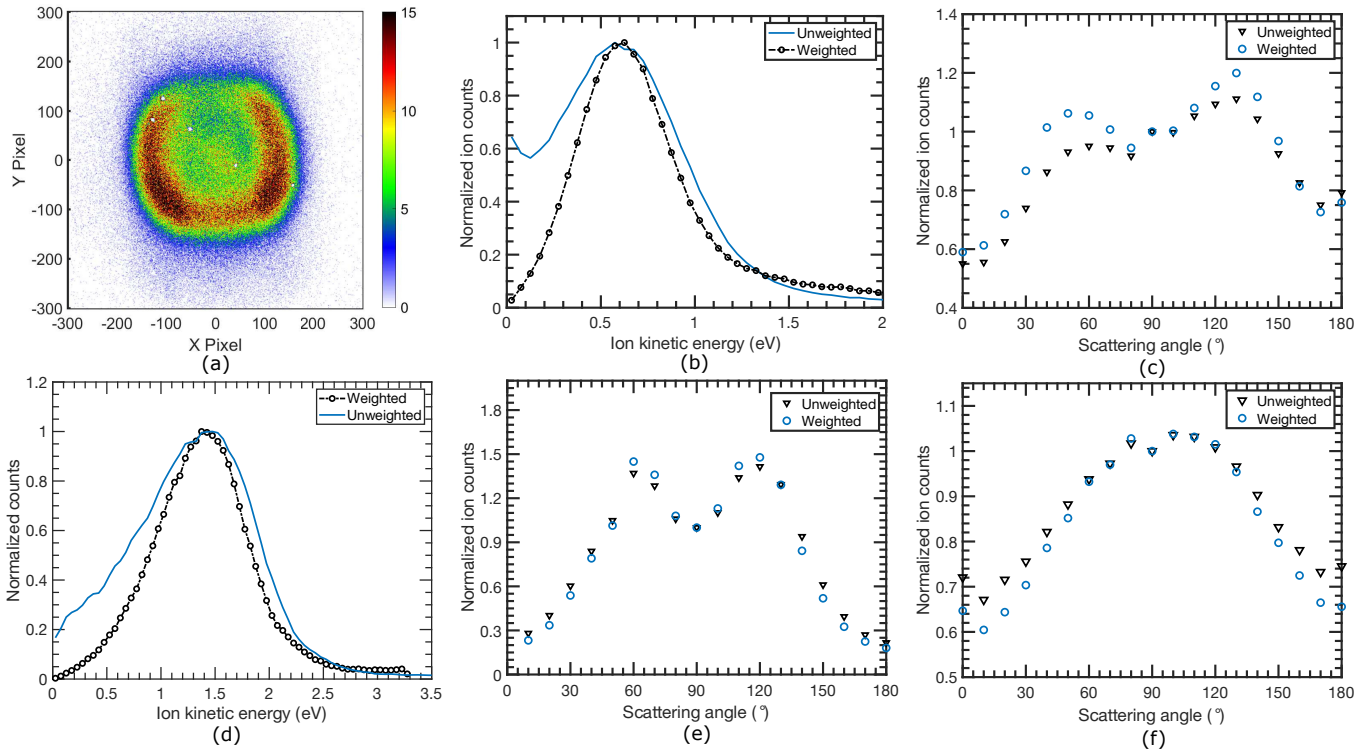

FIG. 2. (a) Time slice image of O^- ions from DEA to CO_2 at 8.2 eV resonance. The electron beam direction is from bottom to top through the center of the image. (b) Comparison of O^- KED, for weighted and unweighted time slices, dissociating from CO_2 at 8.2 eV incident electron energy. (c) Angular distribution comparison for the same CO_2 experimental data as (b). (d) Comparison of O^- KED for weighted and unweighted time slices, for DEA to O_2 at 6.5 eV incident electron energy. (e) Angular distribution comparison for the same O_2 experimental data. (f) Angular distribution comparison of OH^-, for weighted and unweighted time slices, for DEA to ethanol at 9.5 eV incident electron energy.

plitude $f(\theta, \phi)$ is given by:

$$f(\theta,\phi) = \langle \text{Resonant state}|\text{Partial waves}|\text{Initial state}\rangle \tag{1}$$

Here, the components that represent the resonant state and initial neutral state are the basis functions for the irreducible representations of the molecule's point group, and the partial wave denotes the different partial waves of the incoming electrons involved in the transition. This transition amplitude is squared and integrated over the azimuthal angle (ϕ) to obtain the variation of the DEA cross-section ($I(\theta)$) with scattering angle as:

$$I(\theta) = \frac{1}{2\pi}\int_0^{2\pi} |f(\theta,\phi)|^2 \, d\phi \tag{2}$$

Dissociation occurs in the molecular frame, while the angular distribution measurements are carried out in the lab frame. Thus, the transformation of the partial waves from one frame to the other for both the incident electron beam and the electronic states is accomplished using the Euler angles. Such a transformation assumes the dissociating bond does not rotate after the electron attachment and before the dissociation is complete, which is the axial recoil approximation [25]. The expected angular distribution is a combination of the different partial waves of the captured electron. Several research groups have used this method for angular distribution over the years [26, 27], while others [11, 28, 29] have also developed *ab initio* computational methods that require an accurate theoretical description of the bound and continuum electronic structures of the anion.

Nag *et al.* [28] showed a simplified version of the angular distribution ($I_\epsilon(\theta)$) expressed by:

$$I_\epsilon(\theta) \propto \frac{1}{2\pi}\int_0^{2\pi} \left|\sum a_{lm} i^l e^{i\delta_l} X_{lm}(\theta,\phi)\right|^2 d\phi \tag{3}$$

Here, θ and ϕ represent the polar angles of the electron beam in the dissociation frame, and $X_{lm}(\theta,\phi)$ are the basis functions for the irreducible representations of the point group of the molecule expressed in the dissociation frame. The expansion coefficients, a_{lm}, are real numbers, and the phases, δ_l, represent the direct scattering contribution to the electronic part of the process. The values of the indices l and m with a nonzero contribution to the sum in Eq. 3 are restricted by the irreducible representation of the resonant electronic state. The values of a_{lm} reveal the relative contributions of different symmetries of the scattering system and partial waves of the captured electron to the DEA process.

In the ground electronic state, ethanol has planar symmetry, and it belongs to the C_s point group, which is characterized by one horizontal mirror plane. The character table of the C_s point group is shown in Table I. There are two potential irreducible representations within the C_s point group, the one-dimensional $A^{'}$ and $A^{''}$ representations. The $A^{'}$ representation is symmetric to both the identity operator, E, as well as reflection through the mirror plane, σ_h. The $A^{''}$ representation is symmetric to E but antisymmetric for reflection through σ_h. The ground state electronic configuration of ethanol [30] is $(\text{core})^6(4a')^2(5a')^2(6a')^2(7a')^2(1a'')^2(8a')^2(9a')^2(2a'')^2$ $(10a')^2(3a'')^2$, which gives it $A^{'}$ symmetry. By using Eq. 3 and Table I, we deduce the angular distribution function of a C_s point group for the $A^{'} \rightarrow A^{'}$ transition considering the three lowest partial waves as:

$$\begin{aligned} I^{A'}_{(s+p+d)}(\theta) =& \alpha^2_{00} + \alpha^2_{10}\cos^2\theta + \alpha^2_{11}\sin^2\theta \\ &+ \alpha^2_{20}(3\cos^2\theta - 1)^2 \\ &+ \alpha^2_{21}\sin^2\theta\cos^2\theta + \alpha^2_{22}\sin^4\theta \\ &+ 2\alpha_{00}\alpha_{10}\sin(\delta_0 - \delta_1)\cos\theta \\ &+ 2\alpha_{00}\alpha_{20}\sin(\delta_0 - \delta_2)(3\cos^2\theta - 1) \\ &+ 2\alpha_{10}\alpha_{20}\sin(\delta_1 - \delta_2)\cos\theta(3\cos^2\theta - 1) \\ &+ 2\alpha_{11}\alpha_{21}\sin(\delta_1 - \delta_2)\sin^2\theta\cos\theta \end{aligned} \quad (4)$$

On the other hand, the angular distribution function for the $A^{'} \rightarrow A^{''}$ transition considering the lowest two partial waves is

$$\begin{aligned} I^{A''}_{(p+d)}(\theta) =& \alpha^2_{11}\sin^2\theta + \alpha^2_{21}\sin^2\theta\cos^2\theta + \alpha^2_{22}\sin^4\theta + \\ & 2\alpha_{11}\alpha_{21} sin(\delta_1 - \delta_2)\sin^2\theta\cos\theta \end{aligned} \quad (5)$$

In these two equations, $\alpha_{l,m}$ are the rescaled coefficients that include the constant factors. $l = 0, 1$ and 2 indicate the s, p, and d partial waves, respectively. The terms that contain $\alpha_{l,m}\alpha_{l',m'}$ are attributable to the mixing between different partial waves. All the angular distribution data presented in this work are fitted using these two transition models.

III. RESULTS AND DISCUSSION

DEA to ethanol involves TNI electronic states, which dissociate through several fragmentation pathways, including the production of OH^- ions [14, 16, 18]:

$$C_2H_5OH + e^- \rightarrow (C_2H_5OH^-)^* \rightarrow C_2H_5 + OH^- \quad (6)$$

IV. EXPERIMENTAL SET-UP

The ion yield curve shown in Fig. 3 presents two overlapping resonant peaks, a narrow resonance near the 9.5 eV and a small hump near 11.5 eV. Based on the previous DEA studies of ethanol reported by other research groups, the 9.5 eV peak can be assigned to the formation of OH^- ions [13, 14, 16, 18]. We note there is some disagreement in the literature with respect to both the O^- and OH^- DEA resonance energies of ethanol. Using high-resolution mass spectrometry, Ibănescu *et al.* [13, 14] found the resonant peak for O^- and OH^- ions at 10.3 eV and 9.1 eV, respectively. Other high-resolution mass spectrometry experiments reported by Orzol *et al.* [16] determined the O^- resonance to be at 6 eV, and the OH^- resonance at 8.1 eV. In the present work we find good agreement with Refs. [13, 14]. While we cannot separate the OH^- and O^- ions due to the limited mass resolution of the VMI spectrometer, other possible DEA fragments like H^- are excluded due to the higher TOF difference. Hence, Fig. 3 is a total ion yield curve of both the OH^- and O^- ions. Here, we did not observe any resonant peak near 6 eV; however, the hump near 11.5 eV is consistent with the report of Ibănescu *et al.* [13, 14], and can be assigned to the formation of O^- ions. Because of the relatively small cross-section of O^- ions, their signal was not sufficiently high to perform VMI measurements in our system. Therefore, this study focuses only on channels producing OH^-.

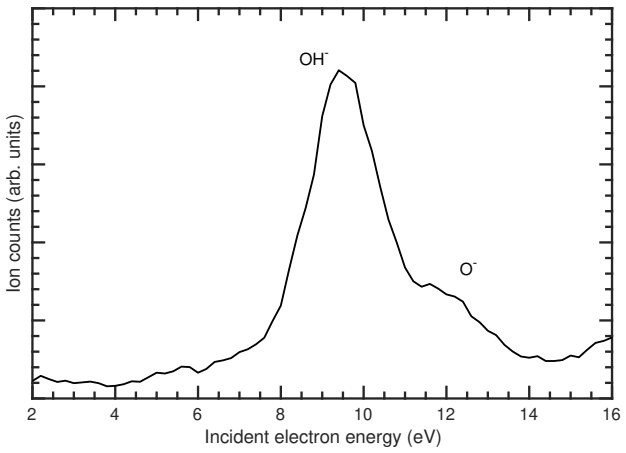

FIG. 3. Ion yield curve of DEA to ethanol. The 9.5 eV peak is assigned to the formation of OH^- ions, whereas the small hump near 11.5 eV is associated with the formation of O^- ions.

A. Kinetic energy distribution

The velocity slice image of OH^- ions at 9.5 eV is shown in Fig. 4. The typical FWHM of the TOF of the OH^- ions produced in this energy range is around 250 ns. A 50 ns time gate was used to record all the images presented in this study, and the center of the time gate is set to the center of the Newton sphere within the experimental uncertainty ($< 10ns$). Considering the resonance energy locations of the O^- and OH^- ions, and their relative cross-sections, we conclude that the contribution from

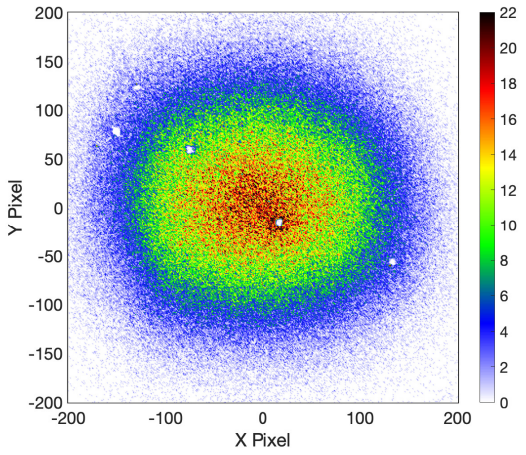

FIG. 4. Time slice image of OH^- ions at 9.5 eV. The electron beam direction is vertically from bottom to top through the center of the image.

O^- ions is negligible below 9.5 eV, and but perhaps significant at higher incident electron energies. The central slice shows the maximum intensity at the center (with a nearly isotropic distribution), which indicates that the kinetic energy of the fragment ions peaks near zero eV. In a process in which low kinetic energy ions are formed, the flat time-sliced image does not accurately reflect the ion KED, as it overestimates the abundance of low-kinetic energy ions [31]. Therefore, we applied a weighted factor, i.e., we multiplied the ion counts by the square of their corresponding distance from the center, to the ion counts to overcome this problem. Prior to the ethanol results, we applied this methodology to the O^- KED of DEA to CO_2 and compared our results with previous measurements, as shown in Fig.2b [31]. Fig. 5 represents the weighted time-sliced images of OH^- ions over different incident electron energies. Here, the incident electron beam direction is from bottom to top through the center of the image for all the energies. One ring pattern can be observed for all the incident energies with a higher ion yield recorded in the perpendicular direction of the incident electron beam. This weighted image shows some anisotropy in the distribution, which was not visible in the unweighted image. In the unweighted slice image, the high abundance of lower kinetic energy ions obscures the anisotropy present in the image. Another reason could be the slightly elliptical shape of the slice image. With the r^2-weighting, the OH^- ion image is correctly weighted to reveal the anisotropy. It is to be mentioned here that identifying the image center is most important in determining the symmetry and anisotropy in each angular distribution, especially when the r^2-weighting technique is applied. To choose the correct image center, we begin by selecting a small circle (e.g. 40-pixel radius) near the center of the unweighted image. This small selection includes many of the events in the transverse plane (orthogonal to the detector plane and e-beam direction). In order to find the center precisely, we compared the integrated ion counts for the left, right, forward, and backward hemispheres (with respect to electron beam direction), for the region enclosed by the small chosen circle in the unweighted image. We shifted the center of that small circle and repeated this process several times until we found the ion count ratio between two hemispheres to be close to unity (typically within 1%). To incorporate the statistical uncertainties, we shift the center by 1 pixel in each direction and measure the deviation caused by this in the angular distribution profile. This deviation is included in the error bar in the angular distribution curves. In order to show that this r^2-weighting technique doesn't alter the angular distribution profile, we compared the AD of the unweighted and weighted OH^- distribution for the 9.5 eV energy, as shown in Fig. 2f. For clarity, we further compared the weighted and unweighted angular distribution of O^- from DEA to CO_2 (at 8.2 eV resonance) and O_2 (at 6.5 eV resonance), as shown in Fig. 2c and Fig. 2e, respectively.

The kinetic energy of the negative ions is extracted from the slice images and shown in Fig. 6. The KED obtained is broad, ranging from 0.1 to 1 eV, and peaking near 0.25 eV for each of the incident electron energies. During the DEA process, the excess available energy (EAE) is distributed as the fragments' kinetic and/or internal energy. The EAE of ethanol can be represented as:

$$\mathrm{EAE} = \mathrm{V}_e - (\mathrm{D} - \mathrm{A}) \tag{7}$$

Here, V_e is the incident electron energy, D is the C-O bond dissociation energy, and A is the electron affinity of the OH radical. If the OH^- ions are formed by a single bond dissociation process (as stated in Eq. 6) then the threshold of this dissociation channel is E_{Th}= (D - A) = 2.22 eV (Considering the OH^- ions are formed at its ground state, D = 4.05 eV,[32], and A = 1.83 eV [33]). In that case, the EAE of the dissociation process at 9.5 eV will be approximately 7.3 eV. This large EAE has to be distributed as (i) the kinetic energy of the fragments, and (ii) their internal excitation. By applying the momentum conservation, the KE of the OH^- ions measured at 9.5 eV is approximately 0.25 eV, which indicates that all of the fragments' total kinetic energy (KE_{Tot}) is:

$$KE_{Tot} = KE_{\mathrm{OH^-}} \times \frac{m_{\mathrm{ethanol}}}{m_{\mathrm{C_2H_5}}} \tag{8}$$

which is approximately 0.4 eV. Here, $KE_{\mathrm{OH^-}}$ is the kinetic energy of the OH^- fragments, $m_{ethanol}$ is the mass of the ethanol molecule and $m_{C_2H_5}$ is the mass of the C_2H_5 fragment. This indicates that if a two-body fragmentation of TNI occurs, only a small portion (5%) of the EAE appears as the fragments' KE, and the remainder is deposited as a rovibrational excitation of the neutrals and the internal excitation of the anion (approximately 95%). The minimal increase in the ion KE peak energy with the increasing incident electron energy further supports this conclusion. However, a small shift can be seen in the KED, which is more prominent in Fig. 6(b). Moreover,

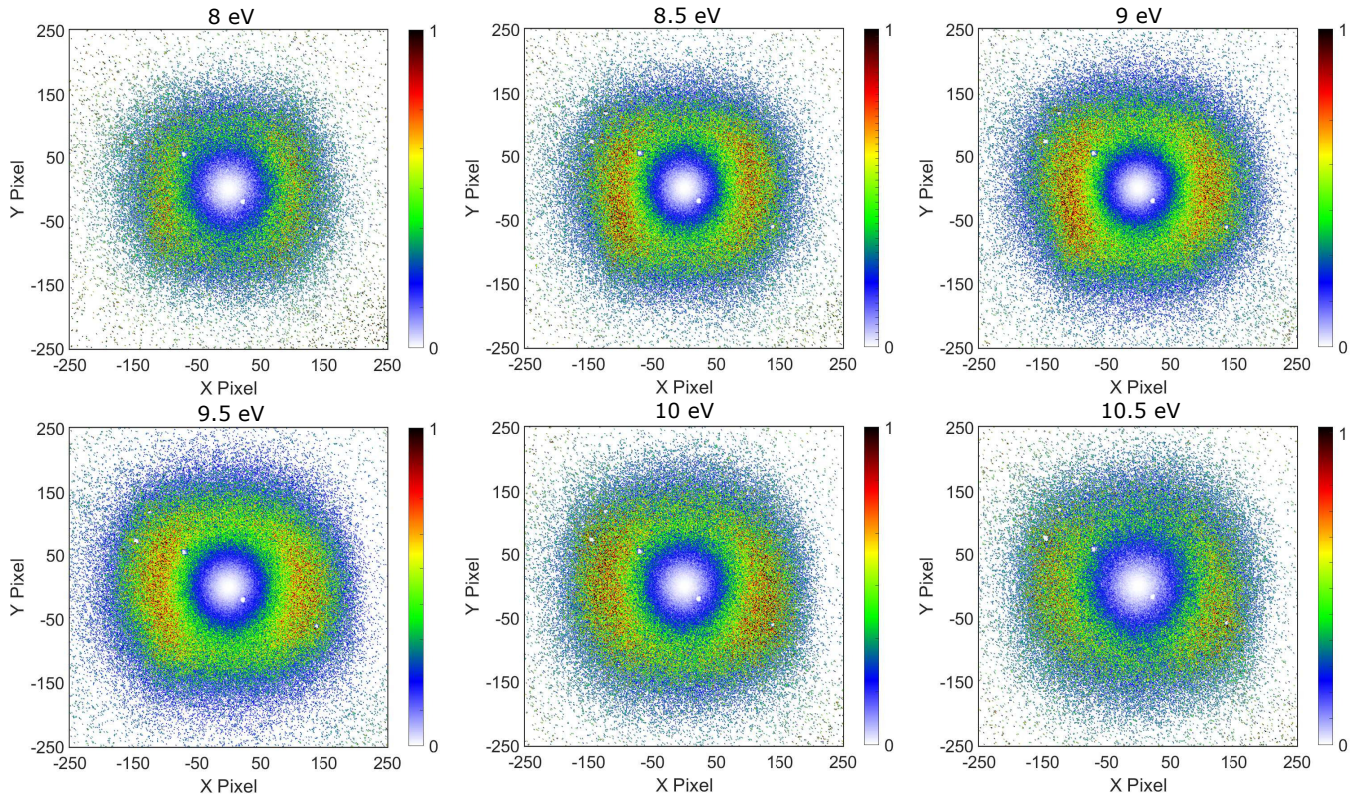

FIG. 5. Weighted time slice image of OH^- ions at several electron energies over the resonance. The electron beam direction is vertically from bottom to top through the center of the image.

the ion KED becomes even broader as the electron energy increases, similarly as was observed in the CH_3O^- KED of DEA to methanol [11]. Our finding indicates that for a two-body fragmentation, the neutral counterpart of the OH^- ions formed in the DEA process are energetically hot, and may dissociate further through a sequential dissociation process. However, based on our experimental results, we are not able to conclude whether a sequential dissociation of the TNI is involved or whether the TNI dissociates through a concerted three-body dissociation process. A high-level theoretical study is required to understand the process or application of experimental methods which are able to detect neutral fragments from DEA [34, 35].

B. Angular distribution

To determine the symmetry of the TNI states involved in the 9.5 eV resonance of ethanol, the angular distribution of OH^- ions was extracted from the VMI images by excluding ions outside of the 0.1 to 1 eV kinetic energy range. Fig. 7 represents the angular distribution of OH^- ions at different incident electron energies. Two angular distribution peaks are visible for nearly all energies with a minimum near 90°. At an electron energy of 8 eV, the two peaks are distinctly visible, and as the electron energy increases, the two peaks become closer. Assuming the axial recoil approximation and following the description given in Section II, we fit the angular distribution data with both the $A' \rightarrow A'$ and $A' \rightarrow A''$transition models.

Figs. 7 and 8 represent the fitted angular distributions for both transition models. The $A' \rightarrow A''$ model gives a poor fit with negative R^2 value, due the significant measured OH^- yield in the forward (0°) and backward (180°) directions. In contrast, the $A' \rightarrow A'$ transition model provides a satisfactory fit to the measured angular distributions. This suggests the TNI has A' and not A'' symmetry. The term α_{lm} denotes the relative contribution of the different partial waves involved in the transition. We found that the p-wave provides the dominant contribution in the transition, along with a small involvement of the s-wave, and d-wave. The s-wave contributes to the angular distribution profile as $l = 0$ and $m = 0$, the p-wave contributes to the angular distribution profile as $l = 1$ and $m = 0$, and 1, and the d-wave contributes as $l = 2$ and $m = 1$. The s-wave p-wave and p-wave d-wave mixing terms also provide contributions to the angular distribution profile. We found that the α_{00}^2, α_{10}^2, α_{11}^2 terms, along with the p-wave d-wave mixing term, $\alpha_{10}\alpha_{20}$, are sufficient to represent the angular distribution profile near the resonance energy of 9.5 eV.

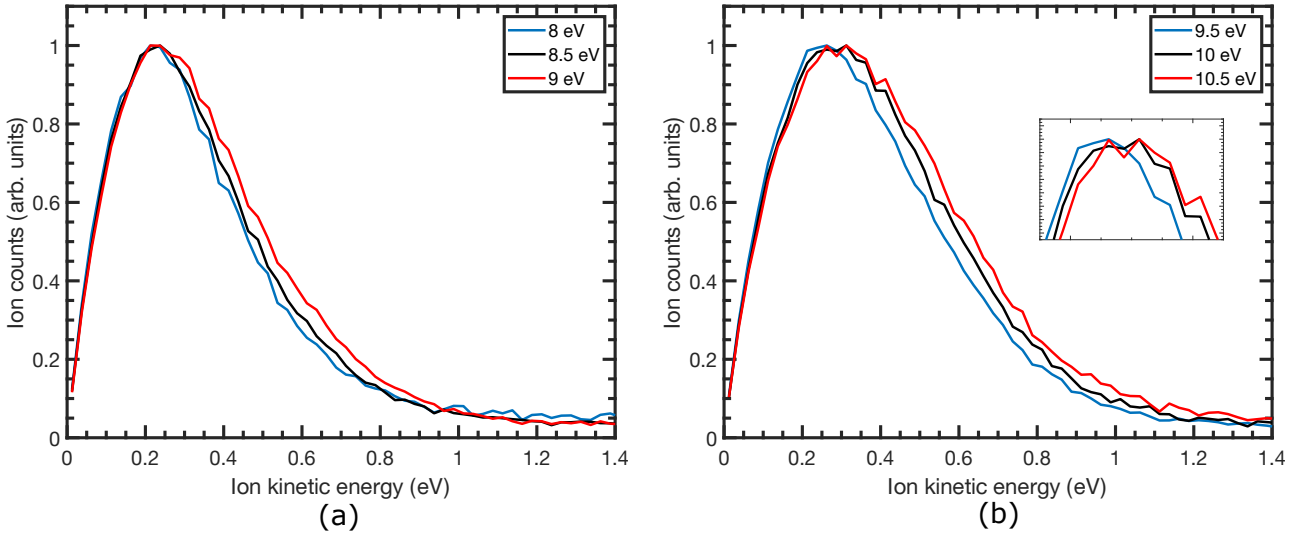

FIG. 6. Weighted KED of OH^- ions at (a) 8, 8.5, and 9 eV, and (b) 9.5, 10, and 10.5 eV. The number of ion counts is normalized to the maximum of the peaks at each energy. The incident electron beam energy indicates the central energy of the incident electron beam and each step is comparable to the electron energy resolution.

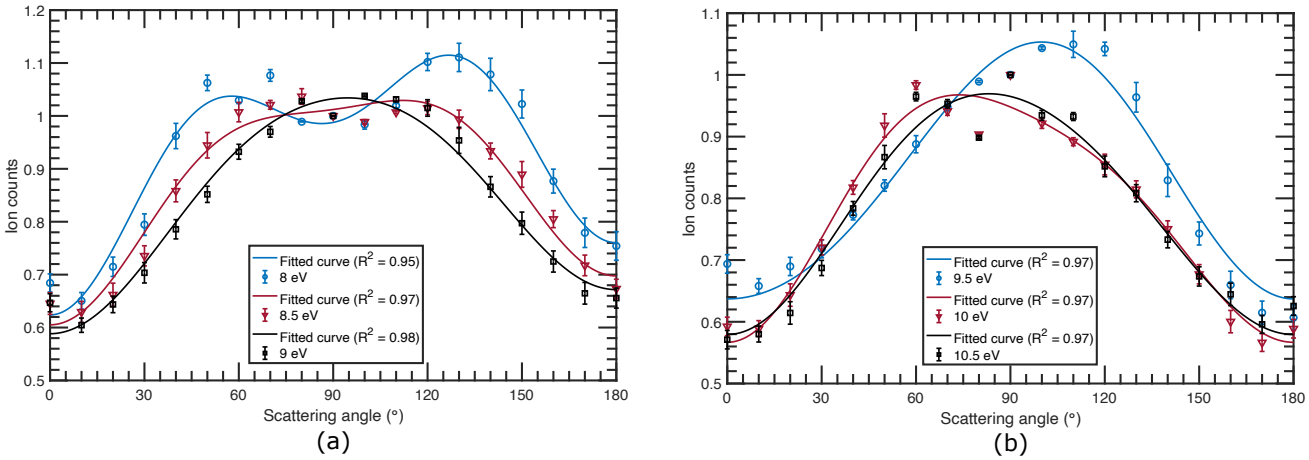

FIG. 7. Angular distribution of OH^- ions (angles with reference to the direction of the electron beam axis) fitted with the $A^{'}$ to $A^{'}$ transition model for (a) 8, 8.5, and 9 eV, and (b) 9.5, 10, and 10.5 eV incident electron energy. The number of ion counts is normalized at 90° angle. The error bar represents the statistical fluctuations of the ion counts.

For energies lower and higher than 9.5 eV, including the d-wave (coefficient α_{21}^2) improves the quality of the fit. In addition, for energies lower than the resonance, the s-wave p-wave mixing term, $\alpha_{00}\alpha_{10}$, results in a better fit than the $\alpha_{10}\alpha_{20}$ term. The other terms in Eq. 4 offer small contributions, and including them in the fit provides a better R^2 value. All the fitting parameters, along with the corresponding R^2 values, are provided in Table II. Based on the fitting, we conclude that the $A^{'}$ TNI state is involved in the resonance formation under the axial recoil approximation; however, any contributions from an $A^{''}$ state cannot be completely ruled out.

To validate these findings, we compare our results with the photoabsorption spectrum of the ethanol molecule studied using VUV synchrotron radiation [36, 37]. That study assigned a $(10a^{'}) \rightarrow 3p(4a^{''})$ Rydberg transition in the 9.5 eV region. This Rydberg state could be the parent state of a Feshbach resonance. In the 9.5 eV Feshbach resonance, the incoming electron loses its kinetic energy to excite the occupied $(10a^{'})$ valence electron and is captured simultaneously with the excited electron in the $(4a^{''})$ orbital, thus giving the TNI state an $A^{'}$ symmetry with an electronic configuration of $[(core)^{22}(10a^{'})^1(3a^{''})^2(4a^{''})^2]$. The photoelectron spectra of ethanol show two ionization processes that correspond to the ionization of the highest occupied molecular

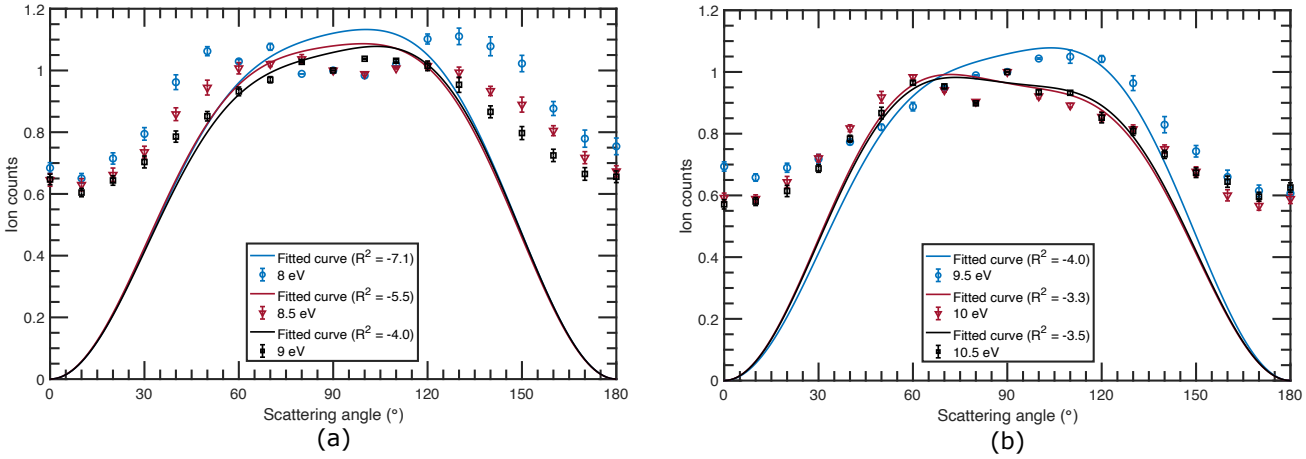

FIG. 8. Angular distribution of OH^- ions (angles with reference to the direction of the electron beam axis) fitted with the $A^{'}$ to $A^{''}$ transition model for (a) 8, 8.5, and 9 eV, and (b) 9.5, 10, and 10.5 eV incident electron energy. The number of counts is normalized at 90° angle. The error bar represents the statistical fluctuations of the ion counts.

orbital (HOMO), i.e., $(3a^{''})$ orbital, at 10.64 eV and the ionization of (HOMO-1), i.e., $(10a^{'})$ orbital, at 12.18 eV [12]. Rydberg transitions, including $(10a^{'}) \rightarrow 3p(4a^{''})$, converging to these ionization potentials occur at lower energies such as 9.5 eV.

The above-mentioned excitation channel of the Feshbach resonance responsible for the DEA to ethanol near 9.5 eV can be further compared with the available literature. Ibănescu *et al.* performed a series of DEA experiments on several alcohols and ethers over the years [13, 15, 38]. Their detailed investigation focused on different DEA resonances that are responsible for different bond dissociation, such as C-H, O-H, C-O, and C-C. By comparing the IE of the neutral molecules, the position of the Feshbach resonances (6.35, 7.85, and 9.18 eV), and by using the empirical formula documented by Spence [39], the authors predicted that the resonances are σ-Feshbach type. Using the theoretical calculations, the authors confirmed that both the 6.35 and 7.85 eV resonances are σ-Feshbach type; however, they found no useful correlation between the σ orbitals and the observed DEA bands near the 9 eV Feshbach region, which takes into account the C-O bond dissociation. Unlike the other channels, the authors observed unexpected trends for the C-O dissociation channel. They performed experiments with ethanol, butyl ethyl ether, ethyl methyl ether, and diethoxy methane, and for all the cases, they observed the presence of the 9.1 eV Feshbach resonance for the ions formed by loss of ethyl neutral counterparts [13]. This observation indicates that the Feshbach resonance position depends only on the neutral fragment, which is formed in the DEA and is independent of the rest of the target molecule. This is surprising because one would expect that the energy of a Feshbach resonance depends on the nature of the entire target molecule, not only on which neutral radical is formed in the fragmentation. Also, such striking selectivity within a dense manifold of highly excited TNI is unexpected, as the individual states are, without doubt, strongly vibronically coupled, allowing the system to jump between the different states through numerous conical intersections. Moreover, this is not only observed for the ethyl radicals but also for other neutral conjugates like propyl, and n-butyl species. This observation indicates there is a connection between the Feshbach resonance responsible for the DEA and the neutral conjugates regardless of the parent molecule. In order to find that connection, the authors compared the resonant energies of the DEA bands with the 1^{st} IE of the associated neutral conjugates and found the energy difference is nearly a constant (3 eV) across a whole range of target molecules. That means the excitation (orbital electrons) in the Feshbach resonances responsible for the DEA bands is localized on the neutral conjugate.

For the 9.5 eV DEA resonance in ethanol, the neutral conjugate (ethyl radical) has an IE near 12 eV, which means the valence electron in the ethanol molecule responsible for the resonant transition should have an IE near 12 eV. In the present case, the assigned $(10a^{'})$ valence orbital has an IE of 12.1 eV [12], which strongly supports our findings about this resonance. Moreover, Spence documented the relationship between the energy of a Feshbach resonance (EF) and the molecules' ionization energy (IE) [39]. The relation is stated as $EF = A.IE + B$, in which the slope, A, has the value one, and the constant, B, has the values of -3.9 and -1.8 eV for the s^2 and p^2 configurations, respectively. The above observation indicates that if a Feshbach resonance is found 4 eV below the IE of the molecule, it could be an s^2-Feshbach resonance, and if it is lying 2 eV below the IE, it could be a p^2-Feshbach. In the present case, the $(10a^{'})$ orbital is involved in the transition with the IE of 12.18 eV [12], and the resonant energy is approximately 9.5 eV. This indicates that the resonance involved

in this transition should be a p^2-Feshbach. The reported photoabsorption spectra also found that a $3p$ Rydberg orbital was involved in this transition [36].

V. CONCLUSION

We investigated the C-O bond dissociation dynamics of DEA to ethanol for the low-energy Feshbach resonance at 9.5 eV, using a velocity map imaging spectrometer. The observed ion yield curve is in good agreement with the previous reports. If two-body dissociation is assumed, the recorded velocity slice images at different electron energies over the resonance revealed that around 95% of the excess available energy of the dissociation process is distributed as a rovibrational excitation of the fragments, whereas only 5% is distributed as the fragments' kinetic energy. We do not rule out the possible involvement of a three-body (or maybe even higher order) dissociation of the TNI. The measured angular distribution of the OH^- fragments exhibits small but significant anisotropy that is consistent with an $A^{'} \rightarrow A^{'}$ electron attachment transition within the axial recoil approximation. Moreover, the angular distribution is consistent with an $A^{'}$ Feshbach resonance, i.e., promotion of an electron from the $(10a^{'})$ HOMO-1 orbital into the $(4a^{''})$ Rydberg-like orbital that is doubly-occupied upon electron attachment. By comparing with photoabsorption spectra [36], our symmetry arguments dictate that the resonance is a p^2-Feshbach type. In a broader aspect, this study provides evidence that p^2-Feshbach resonances could be responsible for DEA in large molecules where the C-O bond dissociates.

VI. ACKNOWLEDGEMENTS

DC and SP are supported by the U.S. Department of Energy Office of Science, Office of Basic Energy Sciences under Award Number DE-FC02-04ER15533 (NDRL No: 5406) for the work performed at Notre Dame Radiation Laboratory. DSS acknowledges the support of the U.S. Department of Energy, Office of Science, Basic Energy Sciences, Division of Chemical Sciences, Biosciences and Geosciences under Contract Number DE-AC02-05CH11231 for the work performed at Lawrence Berkeley National Laboratory.

[1] I. I. Fabrikant, S. Eden, N. J. Mason, and J. Fedor (Academic Press, 2017) pp. 545–657.
[2] S. A. Pshenichnyuk, N. L. Asfandiarov, A. S. Vorob'ev, and Š Matejčík, Physics-Uspekhi **65**, 163 (2022).
[3] E. Böhler, J. Warneke, and P. Swiderek, Chemical Society Reviews **42**, 9219 (2013).
[4] O. Ingólfsson, ed., *Low-Energy Electrons: Fundamentals and Applications* (Jenny Stanford Publishing, New York, 2019).
[5] G. J. Schulz, Rev. Mod. Phys. **45**, 423 (1973).
[6] S. Ptasinska, M. T. d. N. Varella, M. A. Khakoo, D. S. Slaughter, and S. Denifl, Eur. Phys. J. D **76**, 179 (2022).
[7] D. S. Slaughter, A. Belkacem, C. W. McCurdy, T. N. Rescigno, and D. J. Haxton, J. Phys. B **49**, 222001 (2016).
[8] H. Adaniya, B. Rudek, T. Osipov, D. J. Haxton, T. Weber, T. N. Rescigno, C. W. McCurdy, and A. Belkacem, Phys. Rev. Lett. **103**, 233201 (2009).
[9] D. Chakraborty, L. Eckermann, I. Carmichael, and S. Ptasińska, J. Chem. Phys. **153**, 224306 (2020).
[10] M. G. Curtis and I. C. Walker, J. Chem. Soc., Faraday Trans. **88**, 2805 (1992).
[11] D. S. Slaughter, D. J. Haxton, H. Adaniya, T. Weber, T. N. Rescigno, C. W. McCurdy, and A. Belkacem, Phys. Rev. A **87**, 052711 (2013).
[12] S. Thürmer, T. Shinno, and T. Suzuki, J Phys. Chem. A **125**, 2492 (2021).
[13] B. C. Ibănescu and M. Allan, Phys. Chem. Chem. Phys. **11**, 7640 (2009).
[14] B. C. Ibănescu, *ELECTRON-DRIVEN CHEMISTRY OF SATURATED COMPOUNDS CONTAINING OXYGEN OR NITROGEN ATOMS* (Ph.D thesis, Dépertement de Chimie Université de Fribourg (Suisse), 2009).
[15] B. C. Ibănescu, O. May, A. Monney, and M. Allan, Phys. Chem. Chem. Phys. **9**, 3163 (2007).
[16] M. Orzol, I. Martin, J. Kocisek, I. Dabkowska, J. Langer, and E. Illenberger, Phys. Chem. Chem. Phys. **9**, 3424 (2007).
[17] M. M. Fujimoto, W. J. Brigg, and J. Tennyson, Eur. Phys. J. D **66**, 204 (2012).
[18] X.-D. Wang, C.-J. Xuan, W.-L. Feng, and S. X. Tian, J. Chem. Phys. **142**, 064316 (2015).
[19] D. Rapp and D. D. Briglia, J. Chem. Phys. **43**, 1480 (1965).
[20] D. Nandi and E. Krishnakumar, Int. J. Mass Spectrom. **289**, 39 (2010).
[21] D. S. Slaughter, H. Adaniya, T. N. Rescigno, D. J. Haxton, A. E. Orel, C. W. McCurdy, and A. Belkacem, J. Phys. B: At. Mol. Opt. Phys. **44**, 205203 (2011).
[22] R. Azria, Y. L. Coat, G. Lefevre, and D. Simon, J. Phys. B: At. Mol. Phys **12**, 679 (1979).
[23] T. F. O'Malley and H. S. Taylor, Phys. Rev. **176**, 207 (1968).
[24] G. H. Dunn, Phys. Rev. Lett. **8**, 62 (1962).
[25] D. J. Haxton, C. W. McCurdy, and T. N. Rescigno, Phys. Rev. A **73**, 062724 (2006).
[26] D. Chakraborty, A. Giri, and D. Nandi, Phys. Chem. Chem. Phys. **21**, 21908 (2019).
[27] E. Szymańska, V. S. Prabhudesai, N. J. Mason, and E. Krishnakumar, Phys. Chem. Chem. Phys. **15**, 998 (2013).
[28] P. Nag, M. Tarana, and J. Fedor, Phys. Rev. A **103**, 032830 (2021).
[29] G. Panelli, A. Moradmand, B. Griffin, K. Swanson, T. Weber, T. N. Rescigno, C. W. McCurdy, D. S. Slaugh-

ter, and J. B. Williams, Phys. Rev. Res. **3**, 013082 (2021).
[30] Y. Tang, X. Shan, S. Niu, Z. Liu, E. Wang, N. Watanabe, M. Yamazaki, M. Takahashi, and X. Chen, J. Phys. Chem. A **121**, 277 (2017).
[31] A. Moradmand, D. S. Slaughter, A. L. Landers, and M. Fogle, Phys. Rev. A **88**, 022711 (2013).
[32] D. A. Lide, *Handbook of Chemistry and Physics, 78th edn.* (CRC Press, Boca Raton, 1997).
[33] F. Goldfarb, C. Drag, W. Chaibi, S. Kröger, C. Blondel, and C. Delsart, J. Chem. Phys. **122**, 014308 (2005).
[34] S. Ptasinska, Atoms **9**, 77 (2021).
[35] Z. Li, A. R. Milosavljević, I. Carmichael, and S. Ptasinska, Phys. Rev. Lett. **119**, 053402 (2017).
[36] K. Sunanda, A. K. Das, and B. Rajasekhar, J. Quant. Spectrosc. Radiat. Transf. **237**, 106609 (2019).
[37] A. S. Barbosa, M. Mendes, N. Jones, S. Hoffmann, M. Bettega, M. Brunger, and P. Limão-Vieira, J Quant. Spectrosc. Radiat. Transf. **285**, 108170 (2022).
[38] B. C. Ibănescu and M. Allan, Phys. Chem. Chem. Phys. **10**, 5232 (2008).
[39] D. Spence, J. Chem. Phys. **66**, 669 (1977).

TABLE I. Character Table for C_s symmetry group and their respective basis functions for the irreducible representations.

	E	σ_h	Basis Function
$A^{'}$	1	1	$Y_{l,0}$ or $(Y_{l,m} + Y_{l,-m})$; $\forall m$
$A^{''}$	1	-1	$(Y_{l,m} - Y_{l,-m})$; $l, m > 0$, $\forall m$

TABLE II. Fitting parameters for the angular distribution of the OH^- ions arising from DEA to ethanol with the $A^{'} \rightarrow A^{'}$ transition.

Energy (eV)	s-wave	p-wave		d-wave	Mixing coefficients		Phase factors			R^2 value
	α_{00}^2	α_{10}^2	α_{11}^2	α_{21}^2	$\alpha_{00}\alpha_{10}$	$\alpha_{10}\alpha_{20}$	δ_0	δ_1	δ_2	
8	0.155	0.537	0.832	0.836	0.834		0.358	5.048		0.95
8.5	0.055	0.597	0.957	0.419	0.728		0.318	3.954		0.97
9	0.244	0.386	0.789	0.125	0.432		0.099	5.608		0.98
9.5	0.562	0.075	0.478			0.616		4.858	0.159	0.97
10	0.097	0.469	0.851			0.832		0.017	2.784	0.97
10.5	0.059	0.519	0.905	0.107		0.531		1.155	3.71	0.97